

See discussions, stats, and author profiles for this publication at: <https://www.researchgate.net/publication/50248341>

Supramolecular Organization and Charge Transport Properties of Self-Assembled $\pi-\pi$ Stacks of Perylene Diimide Dyes

ARTICLE in THE JOURNAL OF PHYSICAL CHEMISTRY B · MARCH 2011

Impact Factor: 3.3 · DOI: 10.1021/jp111422v · Source: PubMed

CITATIONS

17

READS

14

8 AUTHORS, INCLUDING:



Raphaël Méreau

Université Bordeaux 1

27 PUBLICATIONS 349 CITATIONS

[SEE PROFILE](#)



Laurent Ducasse

Université Bordeaux 1

157 PUBLICATIONS 2,611 CITATIONS

[SEE PROFILE](#)



Frédéric Castet

Université of Bordeaux

90 PUBLICATIONS 1,695 CITATIONS

[SEE PROFILE](#)



Jérôme Cornil

Université de Mons

291 PUBLICATIONS 15,584 CITATIONS

[SEE PROFILE](#)

Supramolecular Organization and Charge Transport Properties of Self-Assembled $\pi-\pi$ Stacks of Perylene Diimide Dyes

Julien Idé, Raphaël Méreau, Laurent Ducasse, and Frédéric Castet

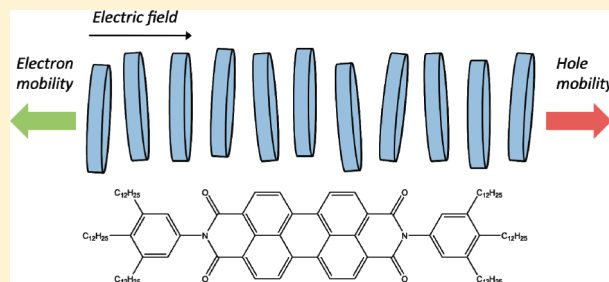
Université de Bordeaux, Institut des Sciences Moléculaires, UMR 5255 CNRS, 351 Cours de la Libération, 33405 Talence, France

Yoann Olivier, Nicolas Martinelli, Jérôme Cornil, and David Beljonne*

Laboratory for Chemistry of Novel Materials, University of Mons, Place du Parc 20, B-7000 Mons, Belgium

 Supporting Information

ABSTRACT: Molecular dynamics (MD) simulations have been coupled to valence bond/Hartree–Fock (VB/HF) quantum-chemical calculations to evaluate the impact of diagonal and off-diagonal disorder on charge carrier mobilities in self-assembled one-dimensional stacks of a perylene diimide (PDI) derivative. The relative distance and orientation of the PDI cores probed along the MD trajectories translate into fluctuations in site energies and transfer integrals that are calculated at the VB/HF level. The charge carrier mobilities, as obtained from time-of-flight numerical simulations, span several orders of magnitude depending on the relative time scales for charge versus molecular motion. Comparison to experiment suggests that charge transport in the crystal phase is limited by the presence of static defects.



1. INTRODUCTION

Due to numerous advantages such as their commercial availability, low cost, or air-stability, columnar crystals and liquid crystals (CLCs) based on perylene tetracarboxylic diimides (PDIs) derivatives have stimulated a large number of studies in the past ten years. These have focused on the use of PDIs as electron-accepting materials in light-emitting diodes^{1–3} or charge transport building blocks in solar cells^{4–11} or organic field-effects transistors.^{12–17} In such materials, disk-like aromatic molecules form π -stacked columnar aggregates, in which the overlap of the π -orbitals of adjacent units yields a one-dimensional pathway for charge migration,^{18,19} leading to charge carrier mobilities comparable to those in amorphous silicon.^{20,21} Moreover, their electronic, optical, and charge transport properties can be tuned over a wide range by changing the aromatic core and the nature and shape of the side groups.^{18,22–27}

Theoretical studies have highlighted the main parameters governing, at the molecular and supramolecular levels, the charge migration in π -conjugated one-dimensional stacks,^{28–32} with an emphasis on the role of geometrical fluctuations. Due to the large degree of structural disorder in these systems (associated with longitudinal/transversal oscillations and rotation motion), the charge transport is expected to operate in a weak-coupling regime, i.e., through a sequence of incoherent hopping processes in which localized charges (polarons) hop between molecules. Modeling charge transport in this limit requires accurate values of the transfer integrals (describing the strength of the couplings between adjacent PDI units) and of the site energies (i.e., the

energy of a charge when it is localized on a particular molecule); these parameters are intimately linked to the morphology of the supramolecular structure and highly sensitive to geometrical fluctuations.

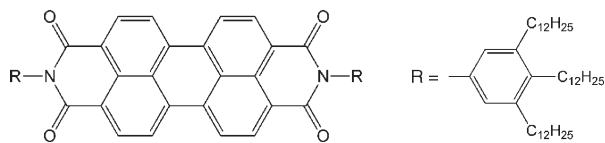
The present study aims at addressing the impact of the structural disorder on the electronic parameters mediating the charge transport properties in columnar stacks of a perylene diimide (PDI) derivative recently characterized by Chen et al.³³ (Scheme 1). This system shows a crystal-LC phase transition at 85 °C, which is accompanied by a decrease of the electrical conductivity by more than 1 order of magnitude. The modeling strategy is similar to that recently used to investigate the structural and hole transport dynamics in various organic semiconductors including self-assembled one-dimensional stacks based on hexabenzocoronene³⁴ or phthalocyanine³⁵ derivatives, and combines classical and quantum-chemical calculations. The supramolecular organization of the PDI molecules in the crystal phase is first investigated by means of molecular mechanics and molecular dynamics (MD) force-field methods. The intramolecular and intermolecular charge transport parameters are subsequently evaluated by applying quantum-chemical methods to snapshots extracted from the MD simulations. Finally, kinetic

Special Issue: B: Shaul Mukamel Festschrift

Received: December 1, 2010

Revised: January 28, 2011

Published: March 01, 2011

Scheme 1. Structure of the PDI Derivative Investigated Here

Monte Carlo simulations are carried out to evaluate the electron and hole mobilities along the PDIs stacks, taking explicitly into account the static and dynamic structural disorder during charge motion.

The structure of this paper is as follows: we describe in section 2 the methodology used to model the morphology of the supramolecular stacks, the way the electronic parameters relevant for charge transport are calculated, as well as our kinetic Monte Carlo implementation to simulate the macroscopic charge carrier mobilities. Section 3 presents the structural arrangement of the molecules in the columns, while the impact of geometrical distortions on the intra- and intermolecular charge transport parameters is discussed in section 4. Finally, we present in section 5 the one-dimensional hole and electron mobilities along the PDI channels by considering different limit cases, with respect to the relative time scales of structural deformations and charge migration.

2. THEORETICAL METHODOLOGY

2.1. Structural Analysis. The supramolecular organization of the PDI stacks has been investigated by means of molecular mechanics and molecular dynamics simulations with periodic boundary conditions using a unit cell containing 13 PDI monomers. MD simulations were carried out in the NPT ensemble at 300 K and 1 atm, for 7 ns with time steps of 1 fs. All calculations were performed using the Tinker package³⁶ and the MM2³⁷ force field. The detailed structural analysis is given in section 3.

2.2. Charge Transport Parameters. The rate of charge hopping between two interacting molecules is given in the framework of Marcus-Jortner theory as^{38,39}

$$k_i^{\text{L/R}} = \frac{2\pi}{h} (J_i^{\text{L/R}})^2 \sqrt{\frac{1}{4\pi\lambda_s k_b T}} \sum_{n=0}^{\infty} \exp(-S) \frac{S^n}{n!} \exp\left[-\frac{(\Delta G_i^{\text{L/R}} + \lambda_s + n\hbar\omega)^2}{4\lambda_s k_b T}\right] \quad (1)$$

where $i = \{1, N_d\}$ with N_d being the number of dimers in the stack. L and R indicate the direction along which the charge jumps along the one-dimensional stacks (respectively left and right; see Scheme 2).

S is the Huang–Rhys factor associated to a single effective intramolecular vibrational mode of energy $\hbar\omega$ (set here to 0.2 eV, typical of C–C bond stretching) that assists the charge transfer by allowing for tunneling across the energy barrier. S is directly related to the internal reorganization energy ($S = \lambda_i/(\hbar\omega)$), that depicts the changes in the geometry of the two molecules involved in the charge transfer process. The internal reorganization energy has been evaluated by using a method based on potential energy surfaces, as the sum of two relaxation contributions:⁴⁰ (i) the difference between the energies of the neutral molecule in its equilibrium geometry and in the geometry of the ion and (ii) the difference between the energies of the radical ion in its equilibrium geometry and in the neutral

geometry. At the B3LYP/6-31G(d,p) level, λ_i is equal to 0.15 and 0.29 eV for holes and electrons, respectively. The external reorganization energy λ_s is governed by changes in the nuclear polarization of the neighboring molecules induced by the charge transfer process, and its calculation is much more tedious.^{41,42} In this work, λ_s has been considered as a tunable parameter with values ranging from 0.05 to 0.30 eV.

$\Delta G_i^{\text{L/R}} = \Delta G_{i,\text{field}}^{\text{L/R}} + \Delta G_{i,\text{disorder}}^{\text{L/R}}$ is the free enthalpy associated to the charge transfer reaction. This energy implies that the energy of the charge is different on the initial and final sites, and results from the application of an external electric field as well as from the presence of energetic (diagonal) disorder. In the case of hole transfer, the contribution of the electric field is given as $\Delta G_{i,\text{field}}^{\text{L/R}} = -|e|\vec{d}_i^{\text{L/R}} \cdot \vec{F}$, with $\vec{d}_i^{\text{R}} (= -\vec{d}_i^{\text{L}})$ the vector connecting the centers of mass of the two molecules in the dimer i . By convention in this work, the field is applied from left to right. Thus, for a hole that migrates in the direction of the field, $\Delta G_{i,\text{field}}^{\text{R}} = -|e|\vec{d}_i^{\text{R}} \cdot \vec{F} < 0$, which tends to increase the charge hopping rate. In the case of an electron transfer, $\Delta G_{i,\text{field}}^{\text{R}} = |e|\vec{d}_i^{\text{R}} \cdot \vec{F} > 0$, so that the migration in the direction opposite to the field is favored.

The contribution of the energetic disorder to the total free enthalpy, $\Delta G_{i,\text{disorder}}^{\text{L/R}}$, is due to the irregular arrangements of the molecules within the columns, and is associated to the change in the polarization energy of the charge carriers during their migration (note that entropic contributions are neglected). This term requires the total electronic energy of a charged molecule within the supramolecular system to be calculated, with an explicit account of electrostatic and polarization effects due to the environment. In the case of holes, the polarization energy is identified as the difference between the ionization potential of a molecule in the stack (IP_{cry}), and the ionization potential of the same molecule in the gas phase (IP_{gas}). Similarly, in the case of electrons, the polarization energy is defined using the electron affinities, EA_{cry} and EA_{gas}

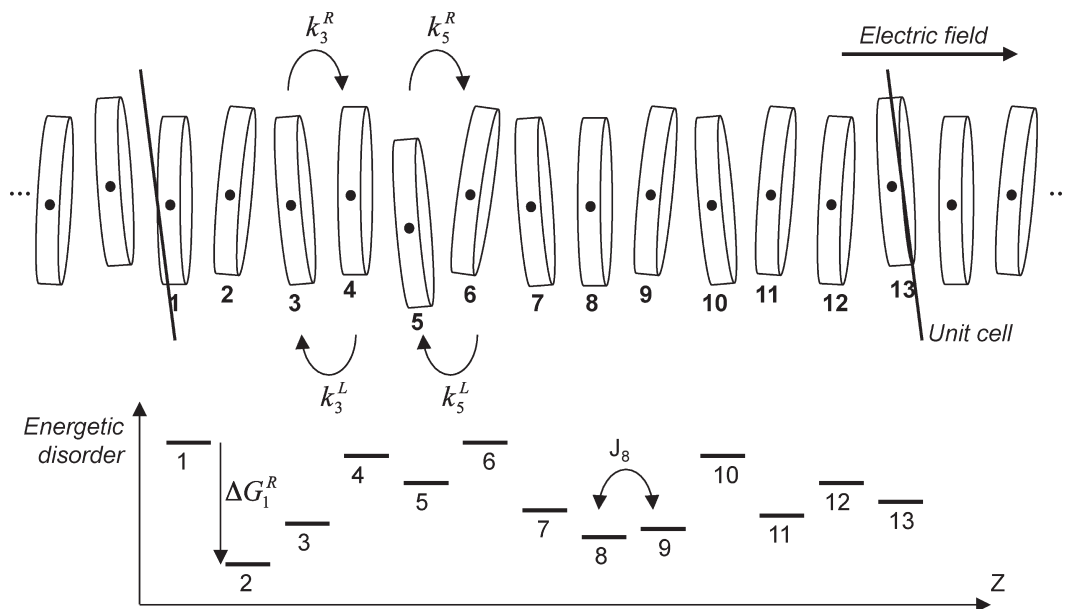
$$P^+ = \text{IP}_{\text{cry}} - \text{IP}_{\text{gas}} \quad (2a)$$

$$P^- = \text{EA}_{\text{cry}} - \text{EA}_{\text{gas}} \quad (2b)$$

Therefore, in the case of holes, the energy disorder is quantified by $\Delta G_{i,\text{disorder}}^{\text{L/R}} = \Delta P_i^{\text{+L/R}}$, where $\Delta P_i^{\text{+L/R}}$ is the variation of the polarization energy when the charge moves from one molecule to the other within the dimer i . Similarly to the electrical field contribution, the $\Delta P_i^{\text{+L/R}}$ and $\Delta P_i^{\text{-L/R}}$ contributions can either be positive or negative, and $\Delta P_i^{(\pm)\text{L}} = -\Delta P_i^{(\pm)\text{R}}$ (see Scheme 2). The $\Delta P_i^{(\pm)}$ terms have been calculated for all dimers within the PDI stacks using the semiempirical valence bond/Hartree–Fock (VB/HF) approach, which allows assessing at the AM1 level the electronic properties of charged molecular units embedded in large supramolecular stacks, while accounting for the interaction of the localized charge with the induced and permanent multipole moments of the surrounding molecules.⁴³

$J_i^{\text{L/R}}$ is the electronic coupling (referred to as the transfer integral) mediating the transfer between the two molecules of dimer i . The terms $J_i^{\text{L/R}}$ have also been calculated for all successive dimers using the VB/HF scheme at the AM1 level, as the couplings between the many-electron wave functions associated to the two charge-transfer states. As discussed in the literature,⁴⁴ these terms are proportional to a weighted sum of the overlap of the orbitals of the interacting molecules, the major contribution arising from the two HOMOs [LUMOs] in the case of hole [electron] transport. Since the electronic distributions in

Scheme 2. Sketch of a PDI Columnar Stack with Molecules and Dimers Labeling (top) and Scheme of the Energetic Disorder along the Stack (bottom)



the HOMO or LUMO levels have been shown to be only slightly perturbed by an electrical field oriented perpendicular to the molecular planes,⁴⁵ the transfer integrals are here assumed to be independent of the electric field, so that $J_i^R = J_i^L = J_i$. As the relative positions of the molecules change from one dimer to another, the transfer integral values strongly fluctuate along the PDI columns, which is referred to as the positional, or nondiagonal disorder.

To account for the effects of dynamical fluctuations, the VB/HF calculations of the polarization energies and transfer integrals were performed on structural arrangements extracted from the force field MD simulations at regular time steps. Though it was recently demonstrated that such a classical sampling underestimates the standard deviation of the electron–phonon couplings at room temperature,⁴² this computational scheme provides a lower limit of the impact of lattice vibrations on the charge transport properties. A total of 800 molecular frames with a time step of 5 ps has been used, which is enough to probe the conformational space of the system.

2.3. Charge Carrier Mobilities. Electron and hole mobilities along the PDI stacks were calculated by simulating the time-of-flight (TOF) experiment using a first reaction method (FRM) approach.⁴⁶ During a TOF measurement, an electric field F is applied between two electrodes where the material is inserted. The charges generated by initial photoexcitation are drifted by the field toward one electrode, and the time-dependent photocurrent is probed. This photocurrent is proportional to the number of charge carriers in the cell. A decrease of this number, thus of the photocurrent, is induced by charge recombination in the irradiated region. The mobility of the holes or electrons is then estimated via

$$\mu = \frac{d}{\tau(|\vec{F}|)} \quad (3)$$

where τ is the time for a charge to cover the distance d separating the two electrodes. In KMC simulations, the total transient time

τ is calculated as the sum of the hopping times $t_i^{L/R}$ for each dimer i , defined as

$$t_i^{L/R} = -\frac{1}{k_i^{L/R}} \ln(u) \quad (4)$$

where u is a random number ($0 < u \leq 1$). For each dimer, the times for the charge to be transferred from one molecule to its left (t_i^L) and right (t_i^R) neighbor are calculated, and the hopping occurs in the direction associated to the smaller time. The total distance covered by the charge in the direction of the electric field is then

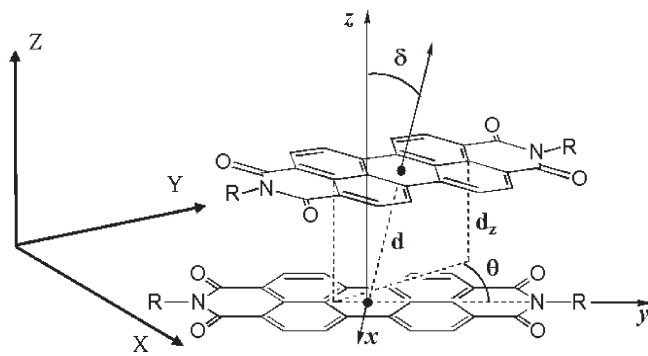
$$d = \sum_{\text{hop}} \vec{d}^{\text{hop}} \cdot \vec{F}_{\text{unit}} \quad (5)$$

where \vec{F}_{unit} is the normalized electric field vector and the sum runs over the number of hopping processes necessary for the charge to cover the distance d .

As every stochastic method, the FRM approach requires a large sample of values (N_{shots}) to converge the simulated properties. On the other hand, the mobility depends on the electric field amplitude, as well as on the distance d that the charge has to travel. Preliminary calculations reported in the Supporting Information have shown that a good compromise between convergence of the computed properties and computational cost is achieved using an electric field of $10\,000\text{ V cm}^{-1}$ and a distance d of 500 nm. The latter corresponds to a charge migration over ~ 110 unit cells, as defined in the periodic MD simulations.

For these F and d values, 50 random snapshots are sufficient to get a reasonable convergence of the average transient time, which is expressed as

$$\langle \tau \rangle = \frac{1}{N_{\text{shots}}} \sum_{i=1}^{N_{\text{shots}}} \tau_i \quad (6)$$

Scheme 3. Structural Parameters Defining a PDI Stack

From $\langle \tau \rangle$, it is then possible to define an averaged mobility

$$\langle \mu \rangle = \frac{d}{\langle \tau \rangle F} \quad (7)$$

However, in a TOF experiment, the charge mobility is usually not extracted from the average transient time, but rather from the time τ_{tr} when the photocurrent starts to decrease (which can be seen as the time for the first charge carrier to recombine at the electrodes).^{47,48} As shown later, τ_{tr} can significantly differ from $\langle \tau \rangle$ in the case of disordered materials. Thus, to simulate in the most realistic way a TOF experiment, where many charge carriers are generated and contribute to the photocurrent, we have assumed that each random shot corresponds to the propagation of a single charge carrier in the cell. Therefore, at $t = 0$, the total number of charge carriers in the material is equal to the total number of random shots used in the KMC scheme, i.e., 50. Knowing the time for each charge carrier to cross the cell, the number of charge carriers remaining into the cell is plotted as a function of time. τ_{tr} is then identified as the time when this number starts to decrease and determined by using a fitting procedure (see section 5).

3. SUPRAMOLECULAR ORGANIZATION OF PDI STACKS

As previously reported, the PDIs investigated here self-organize into a helical arrangement controlled by combination of $\pi-\pi$ interactions between perylene cores and steric effects associated with the end groups, both in the condensed phase²⁷ and in solution.³³ In the helical supramolecular structure, the PDI monomer units are stacked along the Z axis, perpendicular to the planes formed by the perylene cores. As illustrated in Scheme 3, six structural parameters are used to characterize the geometrical structure of the stack:

- (i) the tilt angle δ , which represents the angle between the normal vector of each perylene core and the Z axis
- (ii) the twist angle θ , which measures the rotation of neighboring monomers along the Z axis
- (iii) the distance d between the centers of mass of adjacent perylene cores
- (iv) d_z , the projection of d along the Z axis
- (v) the relative coordinates ΔX and ΔY of the center of mass of each perylene cores, projected onto the XY plane; more precisely, $\Delta X = X_{gi} - X_G$ and $\Delta Y = Y_{gi} - Y_G$, where g_i is the center of mass of the i th perylene core and G the center of mass of the whole system

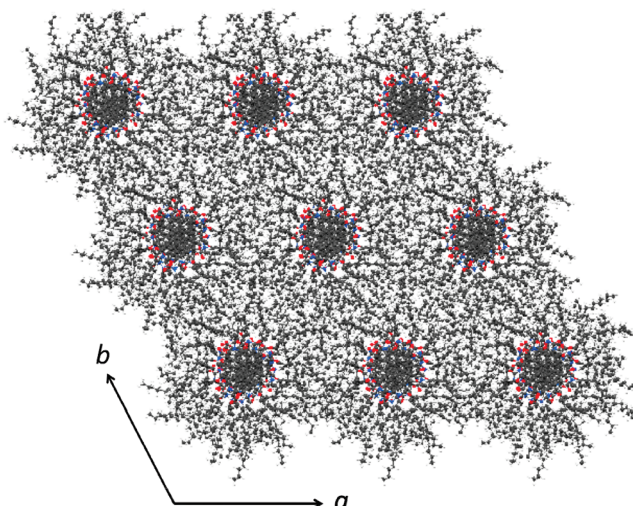


Figure 1. $3 \times 3 \times 1$ supercell of PDI molecules after geometry optimization at the MM2 level, viewed along the Z axis.

- (vi) the relative displacements, Δx and Δy , which correspond to the relative shift of the molecule i in the xyz coordinate system attached to the molecule $i - 1$, where x and y are the short and long axes of $i - 1$, respectively

Preliminary calculations were performed to prepare the PDI samples, as described in the Supporting Information. Geometry optimization yields an hexagonal unit cell with $a = b \neq c$, $\alpha = \beta = 90^\circ$, and $\gamma = 60^\circ$, see Figure 1. On that basis, we have run MD simulations in the NPT ensemble using the Berendsen barostat and thermostat.⁴⁹

Although the temperature stabilizes at 300 ± 2 K after a few picoseconds, the density ρ displays significant variations over a longer period of about 3 ns and then stabilizes with slight fluctuations around an average value of 0.98 g/cm^3 ($\sigma_\rho = 0.003 \text{ g/cm}^3$), as shown in Figure S2 (Supporting Information). The lattice parameters a ($= b$) and c converge to ~ 30.7 and $\sim 40.7 \text{ \AA}$, respectively. For comparison, the crystal structure at 0 K, optimized from 10 snapshots extracted along the dynamics, presents a slightly larger average density of 1.034 g/cm^3 ($\sigma_\rho = 0.005$). The corresponding lattice parameters are $a = b = 29.87 \text{ \AA}$, $c = 40.69 \text{ \AA}$, $\alpha = 90.0^\circ$, $\beta = 89.8^\circ$, $\gamma = 63.2^\circ$ and indicate a compression by about 5.4% of the unit cell compared to the results obtained for the crystal at room temperature. The cell parameter a is in reasonable agreement with the value of 33.5 \AA extracted from X-ray diffraction.³³ The relatively small values of the a and b lattice parameters result from the interdigitation of the alkyl chains between neighboring columns (see Figure 1), as pointed out by Chen et al. for the PDI molecule investigated here or by Percec et al. for similar systems.⁵⁰

The distributions of the relevant structural parameters along the molecular dynamics trajectory (excluding the first 3 ns) are given in Figure 2. The tilt angle δ (Figure 2a) shows a distribution centered around 3.65° . The small values calculated for this angle indicate that the perylene cores remain very close to a cofacial configuration during the MD run. The twist angle θ (Figure 2b) follows a Gaussian distribution, peaking at 55.4° , which confirms the relative orientation of adjacent monomers estimated by Chen et al. from comparison between experimental and theoretical absorption spectra.³³ The projection of the centers of mass of the molecules in the XY plane (Figure 2c) displays a small dispersion ($\pm 2 \text{ \AA}$) around the superimposed

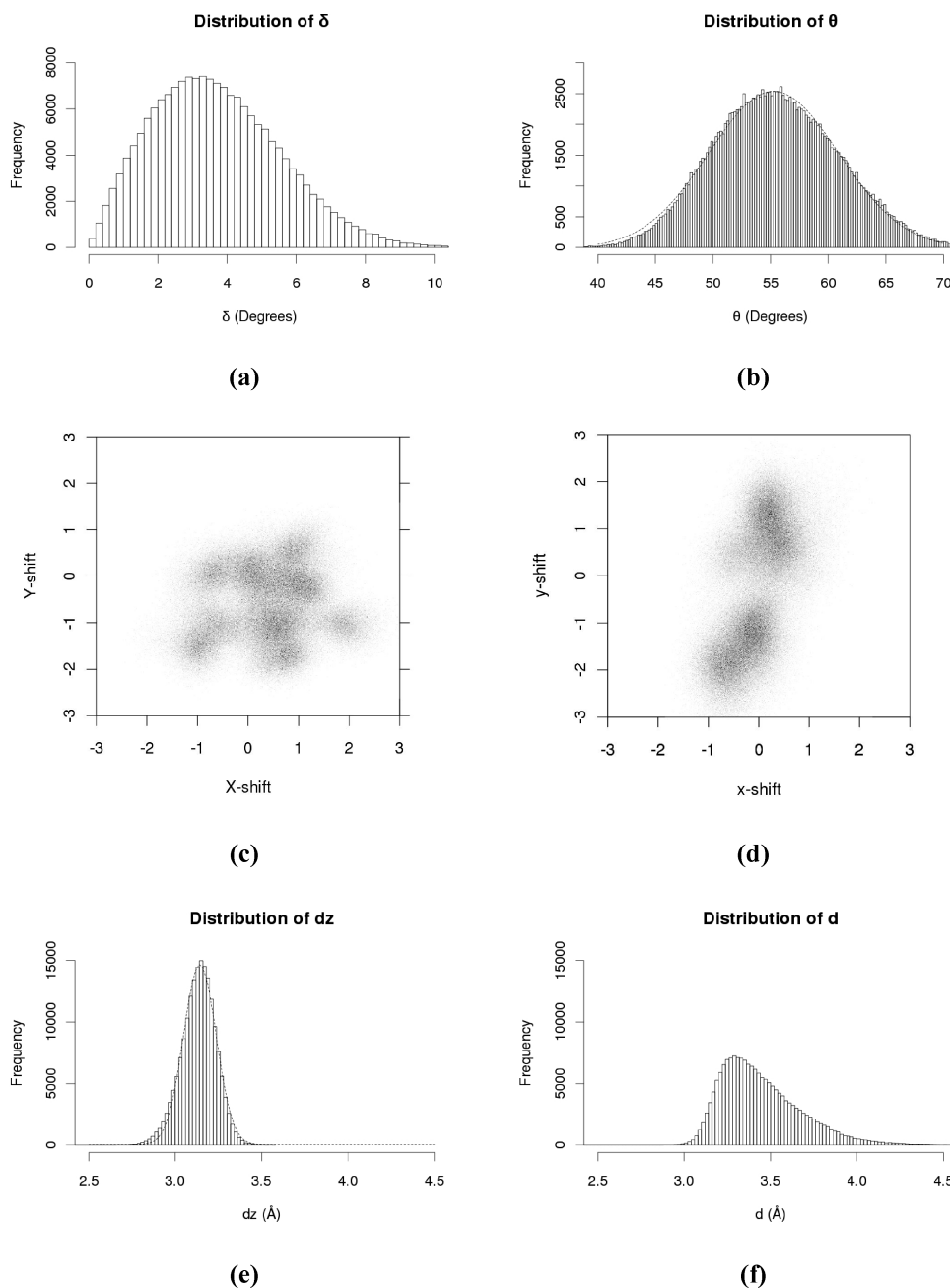


Figure 2. Distribution of the structural parameters values along the MD simulation. A fit to a Gaussian distribution is performed for d_z and θ .

arrangement (which corresponds to the $[0, 0]$ point on the plot), consistent with the formation of H-like aggregates generally observed for PDI derivatives with linear alkyl chains at the periphery.⁵¹ The distribution of the relative shifts (Figure 2d) is larger along the y axis than along the x axis. This originates from the steric hindrance imposed by the phenyl groups at the edge of the perylene cores, which reduces the possibility for the molecule to shift longitudinally along the x axis; as a consequence, lateral displacements along the y axis of the molecules are mainly observed. Finally, the packing distance d_z between the neighboring perylene cores (Figure 2e) features a Gaussian distribution with a maximum at 3.13 \AA , while an asymmetric shape is obtained for the histograms reporting the distance d between the centers of mass of adjacent molecules (Figure 2f).

4. CHARGE TRANSPORT PARAMETERS

The polarization energies and transfer integrals of the charge carriers have been calculated using 800 different atomic positions saved every 5 ps during the last 4 ns of the MD simulations, via the procedure described in section 2.2. To enable sampling of the whole supramolecular conformational space of the PDI stacks, a large number of VB/HF calculations have been performed. For practical reasons, the system was simplified (i) by using a reduced number of molecular units in the columns and (ii) by reducing the length of the lateral substituents. We have performed preliminary test calculations in order to identify representative cluster sizes and lateral groups that provide the best compromise between accuracy and computational time. The results of these calculations are detailed in the Supporting Information and

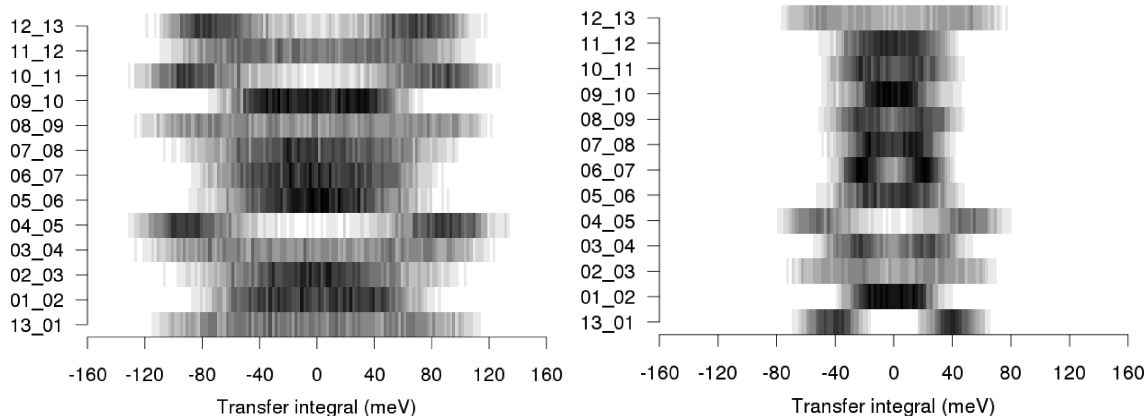


Figure 3. Transfer integral distributions for adjacent molecular pairs in the stack for holes (left) and electrons (right), as calculated at the VB/HF-AM1 level.

indicate that a cluster of 5 units is large enough to include the largest part of the polarization effects on IP and EA, while the transfer integrals can be calculated on dimers. Replacing the lateral substituent R (see Scheme 1) by a simple phenyl group results in relatively small errors on the electronic properties of interest (by up to 0.55% for IP, 6.20% for EA, 6.03% for J^+ , and 7.40% for J^-).

4.1. Polarization Energies. As discussed in section 2, the energy disorder $\Delta G_{i,\text{disorder}}^{L/R}$ for hole (electron) migration is associated to the change in the electronic polarization energy P^+ (P^-) when a positive (negative) charge migrates along the stack. The distributions of P^+ and P^- are reported in Figure S7. All distributions display a Gaussian shape, with mean values ranging between ~ -0.1 and ~ -0.2 eV for P^+ , and between ~ 0.2 and ~ 0.3 eV for P^- . Note that the positive sign of P^- is related to the sign of the electron affinities, which by convention are positive in this work. The average standard deviations calculated for P^+ and P^- are similar and equal to 0.04 eV, which indicates that the on-site energies for hole and electrons, although local in nature, are significantly impacted by the structural distortions of the environment.

As detailed in ref 43, the polarization energies P^\pm can be further decomposed into a purely electrostatic contribution S^\pm and a contribution due to the orbital relaxation, referred to as the dynamic polarization energy D^\pm . The S^+ (S^-) term yields the difference in IP (EA) between the isolated fragment and the same fragment in electrostatic interactions with a molecular environment, while the dynamic electron polarization contribution D^+ (D^-) yields the change in IP (EA) induced by the electronic cloud reorganization. The distributions of the S and D contributions are reported in the Supporting Information. S^+ and S^- display very similar distributions, with values oscillating along the stack between 0.05 and 0.25 eV. On the other hand, the D^+ and D^- distributions strongly differ from each other, with average values of -0.25 eV for D^+ and of 0.12 eV for D^- . Moreover, the distributions related to the dynamic polarization energies are much narrower than those obtained for the electrostatic contributions. This originates from the fact that the D^\pm contributions are mostly correlated to the distance d_z between aromatic cores, which itself displays a very narrow distribution. On the contrary, the S^\pm contributions reflect mostly the interactions between the quadrupolar charge distributions associated with the diimide units. As these depend on many structural parameters, among which the tilt and twist angles, broader energetic distributions are found.

4.2. Transfer Integrals. Figure 3 portrays the population of transfer integrals J^+ and J^- between adjacent PDI units in the unit cell, as probed at the VB/HF level along the MD trajectory. Due to the arbitrary sign of the transfer integrals (that depend on the phase convention for the individual wave functions), the J^+ and J^- histograms display two bands of Gaussian shape symmetrically distributed around zero. It is noteworthy that the transfer integral distributions for holes are more scattered than the electronic counterpart, indicating that the overlap between the HOMO wave functions is more sensitive to geometrical fluctuations. Indeed, the absolute values of the transfer integrals related to holes range between 0 and 100 meV, while they range between 0 and 50 meV for electrons. We also note that the transfer integrals provided by the VB/HF calculations are much smaller (by up to 1 order of magnitude) compared to the corresponding values obtained recently by Vura-Weis et al.⁵² in similar systems using the energy-splitting in dimer method⁴⁴ at the DFT level. A similar discrepancy has been reported for molecular solids involving $\pi-\pi$ interacting fragments such as organic conductors,⁵³ as well as in DNA strands,⁵⁴ and originates from the use of a minimal Slater-type basis set at the AM1 level. Since INDO has been shown to provide electronic couplings for holes and electrons in better agreement with ab initio and DFT methods,⁵⁵ complementary calculations were carried out at this level of approximation, and are reported in the Supporting Information. It is found that the INDO transfer integrals are 3.5 times larger than the VB/HF ones, with the two levels of calculation leading to very similar distributions.

We also stress that the shape of the distribution varies from one molecular pair to the other along the stack, evidencing a large disorder. These variations might be seen as an artifact due to the fact that only one MD trajectory has been used to generate the coordinate samples. However, this does not affect KMC simulations, since (i) a large number of random snapshots are generated to estimate the charge carrier mobilities, (ii) the distance covered by the charge (500 nm) corresponds to more than one hundred unit cells, and (iii) the original molecule (i.e., the molecule bearing the charge at $t = 0$) is chosen randomly within the unit cell.

4.3. Dependence of the Transfer Integrals on the Structural Parameters. In order to get further insight into the impact of changes in the supramolecular arrangements on the transfer integrals, additional calculations have been performed to investigate systematically the evolution of J^+ and J^- with the structural

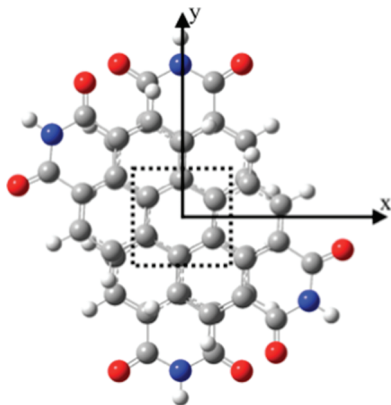


Figure 4. Structure of the model PDI dimer.

parameters defined in Scheme 3. A model dimer constituted of two perylene cores (with $R = H$) separated by 3.2 \AA with a rotation angle of 55° (which corresponds to the mean values of d_z and θ along the dynamics) has been considered (Figure 4). As previously mentioned, the main contribution to J^+ (J^-) corresponds to the coupling term between the HOMOs (LUMOs) of the two facing molecules. The overlap between the frontier orbitals is conditioned by their relative position, characterized by the twist angle θ , the tilt angle δ , and the Δx and Δy shifts. The evolution of the transfer integrals with respect to variations of these four parameters is investigated in this section.

Evolution of J^+ and J^- with θ . Figure 5 reports the evolution of the absolute values of the transfer integrals with respect to θ . Both J^+ and J^- are very sensitive to the θ angle, and can be switched off for particular values of θ . It is interesting to notice that in the range explored by θ during the dynamics (see histogram in Figure 5), J^+ and J^- behave differently: J^+ varies from 100 to 50 meV with a maximum at 110 meV, while J^- varies almost linearly from 0 to 75 meV.

Evolution of J^+ and J^- with Δx and Δy . The variations of J^+ and J^- with respect to the Δx and Δy shifts are illustrated in Figure 6 (θ is kept constant at 55°). The two color maps allow rationalizing the distributions of the J^+ and J^- values reported in Figure 3 for the various molecular pairs. As a representative example, we consider here the transfer integrals between molecules 7 and 8. The distributions of the J^+ and J^- values for this particular dimer are reported in the lower panel of Figure 6, whereas the values of the relative shifts Δx and Δy sampled along the dynamics are superimposed to the color maps of J^+ and J^- . For electrons, the distribution of the relative lateral displacements covers a region where the J^- values vary from 0 to about 50 meV, while in the case of holes, J^+ displays larger variations (from 0 to about 100 meV). Therefore, the fluctuations in J^+ and J^- as the molecules explore the $[\Delta x, \Delta y]$ space phase during the MD run are held responsible for the large differences between the J^+ and J^- distributions reported in Figure 3.

Evolution of J^+ and J^- with Δx , Δy , θ , and δ . We have investigated the impact of simultaneous changes in Δx , Δy , and θ on the transfer integrals. These maps are reported in Figure S14 (see also the animated maps provided in the Supporting Information). One observes that changing the value of θ induces more significant variations on the J^+ than on the J^- counterpart. These variations reinforce the differences in the landscape of J^+ and J^- , and participate in the large differences in the distributions observed above.

Despite the fact that δ does not display large variations along the MD samplings, we have also addressed the influence of this structural parameter on the transfer integrals. In fact, two different tilt angles were considered, corresponding to rotations around the x and y axes. The rotational angles R_x and R_y vary between 0 and 12 degrees along the dynamics. The variation of J^+ and J^- with R_x and R_y can be visualized on the corresponding animated maps provided in Supporting Information, as well as in Figure S15 and S16. In the domain explored by δ , at $\Delta x = \Delta y = 0$, J^- changes from 50 to 60 meV and J^+ changes from 115 to 130 meV. Thus, in the absence of Δx and Δy shifts, the variations of J^+ and J^- due to δ are negligible. For larger relative shifts, more pronounced variations of J^+ and J^- are observed; the geometries correspond, however, to less probable Δx and Δy values.

5. CHARGE CARRIER MOBILITIES ALONG THE PDI STACKS

The hole and electron mobilities have been calculated using the KMC procedure described in section 2.3, by considering different limiting cases. In the first case, we consider that the nuclei are frozen during the migration of the charge carriers. In this case, referred to as the static limit, the charge transfer rates used in the KMC simulations are calculated using the values of the intermolecular distances ($d_i^{L/R}(t)$) and charge transport parameters $J_i^{L/R}(t)$ and $\Delta P_i^{(+/-)L/R}(t)$ evaluated for each dimer i at each time step t of the molecular dynamics (i.e., using the atomic positions saved every 5 ps along the MD run). This limit corresponds to the situation in which the structural deformations of the stacks are slow in comparison to the charge transport.

In the case where fluctuations in the supramolecular arrangement of the 1D columns occur on time scales that are commensurate with the inverse charge hopping rates, the static picture above does not hold any longer and dynamical disorder has to be taken into account. This can be modeled in different ways:

- (i) by using a time-averaging procedure where the charge transfer rates are calculated using, for each dimer, charge transport parameters time-averaged over the entire MD run

$$\begin{aligned} J_i^{L/R} &= \frac{1}{N_{\text{frames}}} \sum_{t=1}^{N_{\text{frames}}} J_i^{L/R}(t) \\ \Delta P_i^{(+/-)L/R} &= \frac{1}{N_{\text{frames}}} \sum_{t=1}^{N_{\text{frames}}} \Delta P_i^{(+/-)L/R}(t) \end{aligned} \quad (8)$$

- (ii) by using a space-averaging procedure where site energies and transfer integrals are spatially averaged over the 13 dimers of the unit cell at any given time t :

$$\begin{aligned} J^{L/R}(t) &= \frac{1}{N_{di=1}} \sum_{di=1}^{N_d} J_i^{L/R}(t) \\ \Delta P^{(+/-)L/R}(t) &= \frac{1}{N_{di=1}} \sum_{di=1}^{N_d} \Delta P_i^{(+/-)L/R}(t) \end{aligned} \quad (9)$$

- (iii) combining (i) and (ii) above where the hopping rate is computed for a single time- and spatially averaged value of the transfer integral and site-energy.

It is clear that scenarios (i) and (ii) should converge to (iii) in the ergodic limit, where all molecules in phase space have the same time distribution. This is not necessarily the case here as one

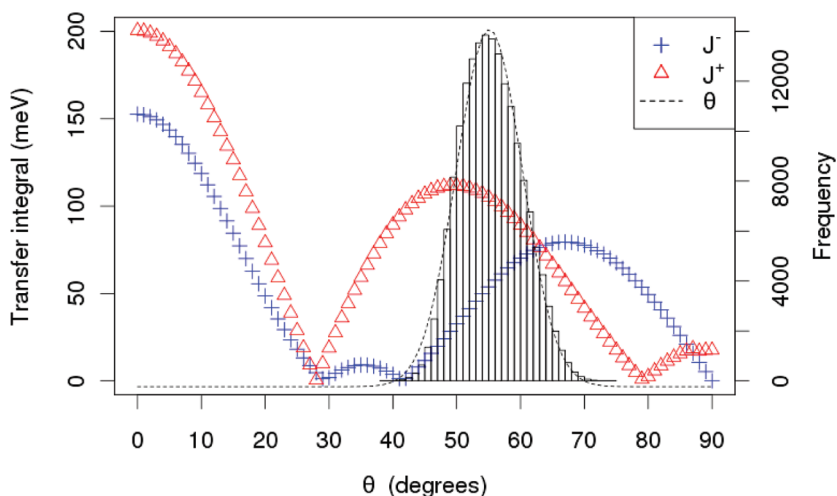


Figure 5. Evolution of J^+ and J^- as a function of θ . The histogram represents the distribution of θ along the dynamics.

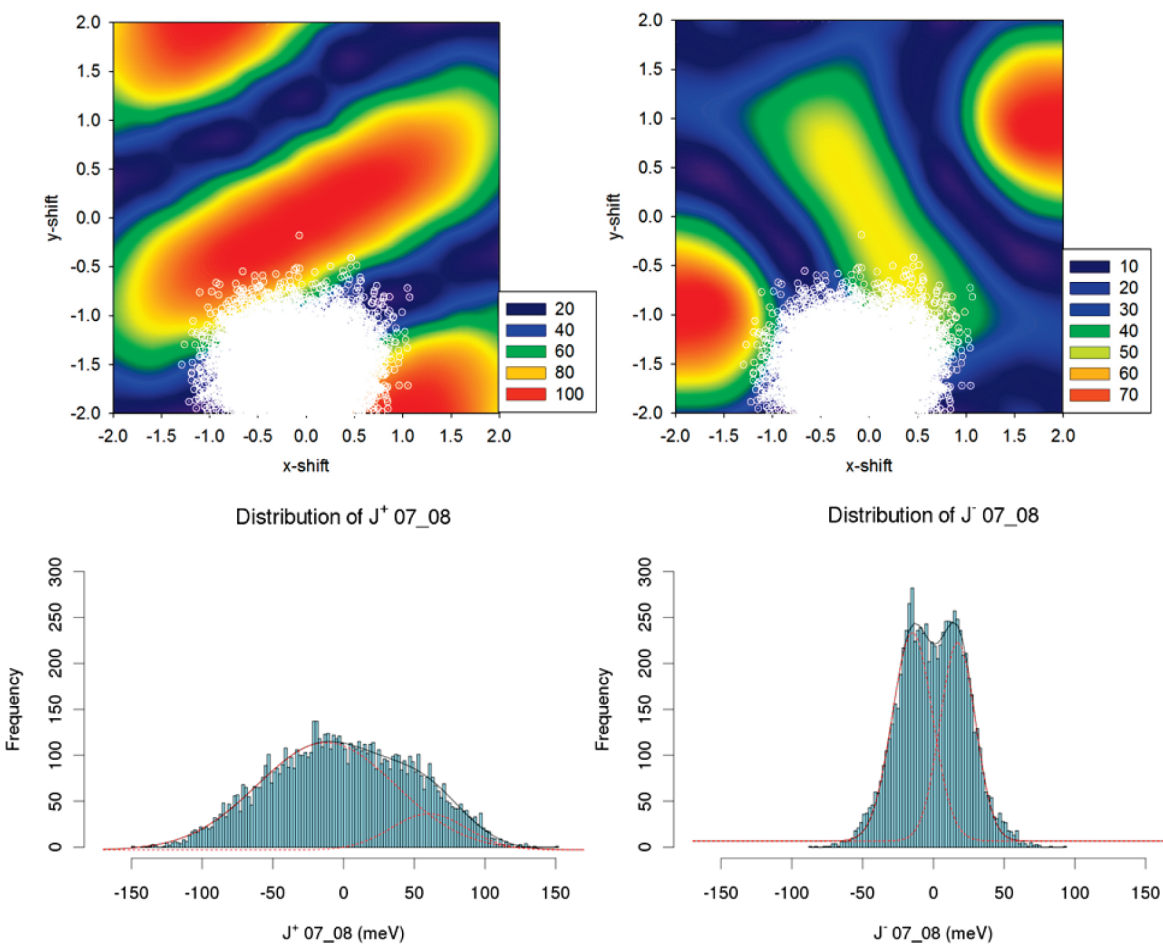


Figure 6. Evolution of J^+ (left) and J^- (right) (in meV) with Δx and Δy (top) in the model dimer, and transfer integral distributions extracted from the MD simulations for a charge migration between molecules 7 and 8 (bottom).

might anticipate that some of the fluctuations in the relative molecular positions take place on time scales that are long in comparison to a TOF numerical simulation. We have thus considered the three different limiting cases in the following.

5.1. Charge Carrier Mobilities in the Static and Dynamic Limits.

The charge carrier mobilities calculated in the various

limiting cases using the VB/HF and INDO transfer integrals are reported in Table 1, for different values of the external reorganization energy. Figure 7 displays, in a log–log plot, the evolution of the number of charge carriers in the cell as a function of time as obtained in the static, time-averaged, space-averaged and space-and-time-averaged limits. As mentioned in section 2.3,

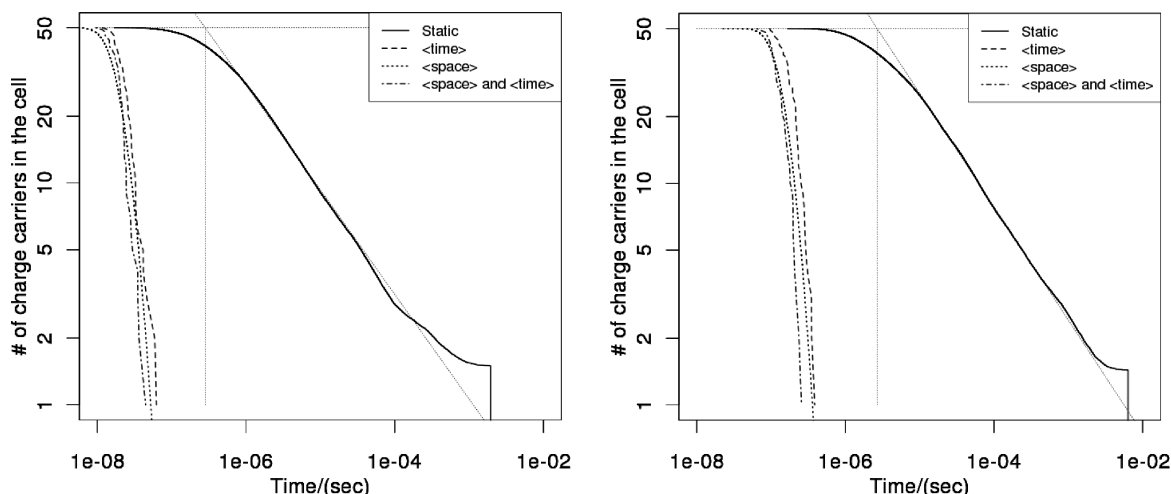


Figure 7. Evolution of the number of charge carriers in the cell as a function of time in the static, time-averaged, space-averaged and space-and-time-averaged limits, in the case of holes (left) and electrons (right) for $\lambda_s = 0.20$ eV.

the transient time τ_{tr} is defined as the time when the number of charge carriers in the cell starts to decrease due to collection at the electrode, and is deduced from the intersection of the two linear asymptotes related to the two regimes of the photocurrent.

We note first that although PDIs are known as good candidates for electron injection due to their high electron affinity, the hole mobilities are 1 order of magnitude larger than the electron mobilities. Thus, PDIs provide a good illustration on how materials selected for their ability to inject charges are not necessarily optimized for charge transport. Moreover, as expected, the mobilities calculated using the INDO transfer integrals are larger than those obtained using the VB/HF transfer integrals. $\mu_{INDO}/\mu_{VB/HF}$ ratios of 10.28 and 12.33 are respectively found for holes and electrons, consistent with the ratio of 3.5 between the INDO and VB/HF electronic coupling terms (as μ scales with t^2).

As shown in Table 1, the static case provides a lower limit for the charge mobilities. In this case, charge migration is indeed very sensitive to the presence of sites with lower or higher energy that act as trapping or scattering sites. Those effects are of course attenuated in presence of dynamic fluctuations, hence the higher μ values. We also observe in Figure 7 that the decrease of the photocurrent is quite progressive in the static limit (with slopes of the linear fits of 3.07×10^{-7} and $2.56 \times 10^{-6} \text{ s}^{-1}$ for holes and electrons, respectively), a characteristic of dispersive motion in disordered materials. Note that calculations using the average transient time $\langle \tau \rangle$ instead of τ_{tr} (see section 2.3) would lead to significantly different charge mobility values (3.28×10^{-4} and $5.70 \times 10^{-5} \text{ cm}^2 \text{ V}^{-1} \text{ s}^{-1}$ for holes and electrons respectively). Charge carrier mobilities calculated with $\langle \tau \rangle$ for each limiting case and values of λ_s are given in Table S5.

The difference between τ_{tr} and $\langle \tau \rangle$ is attenuated when accounting for dynamic fluctuations that in essence wash away the energetic and positional disorder. As can be seen from Figure 7, the photocurrent decreases indeed much more abruptly in the various dynamic limits; in addition, τ_{tr} is shifted toward shorter time values, consistent with larger charge carrier mobilities.

The time-evolution of the photocurrent obtained in the time-and-space- versus time- or space-averaged limits are quite similar, which indicates that the system is almost ergodic. For a perfectly ergodic system, the charge carrier mobility values reported in

Table 1. Charge Carrier Mobilities (in $\text{cm}^2 \text{ V}^{-1} \text{ s}^{-1}$) in the Various Limiting Cases, as Calculated with the KMC Scheme using the VB/HF or the INDO Transfer Integrals

λ_s	VB/HF				INDO
	0.05	0.10	0.20	0.30	0.20
Static Limit					
μ_{h+}	0.1397	0.0493	0.0162	0.0046	0.3254
μ_{e-}	0.0109	0.0062	0.0019	0.0007	0.0319
Time-Averaged Limit					
μ_{h+}	1.9795	0.8328	0.2474	0.0692	2.5806
μ_{e-}	0.2307	0.1048	0.0295	0.0094	0.3893
Space-Averaged Limit					
μ_{h+}	2.6511	1.1301	0.3050	0.0951	3.7861
μ_{e-}	0.3542	0.1577	0.0388	0.0118	0.5301
Time-and-Space-Averaged Limit					
μ_{h+}	2.4758	0.9468	0.3091	0.1013	3.6390
μ_{e-}	0.3142	0.1564	0.0416	0.0116	0.5081

Table 1 in the time-, space-, and time-and-space-averaged limits should be exactly identical. The small residual differences are related to the fact that on a time scale of a TOF simulation or experiment, the charges do not explore the entire distribution of site energies and couplings.

5.2. Influence of the Reorganization Energy. The evolution of the mobility as a function of the external reorganization energy is illustrated in Figure 8. As expected from the definition of the Marcus transfer rates, the increase of λ_s implies a larger energy barrier for charge carriers and thus reduces their mobility. Whatever the limiting case, increasing λ_s from 0.05 to 0.10 eV induces a decrease of the mobility by about 60%. This evidence the dramatic role of the reorganization energy in the efficiency of the charge transfer processes, and the need for more advanced quantum-chemical methods allowing accurate estimates of this parameter. We also stress that, similarly to the internal reorganization energy, λ_s should depend on the nature of the charge carrier. Therefore, the direct comparison of the electron and hole mobilities in Table 1 is biased by the fact that the same value of λ_s

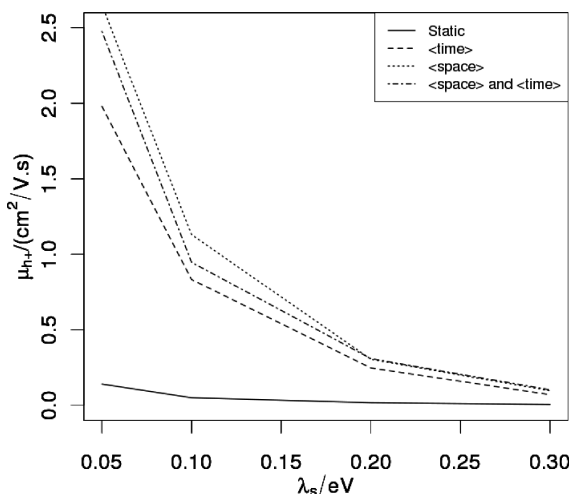


Figure 8. Hole mobility as a function of the external reorganization energy in the static, time-, space-, and time-and-space-averaged limits.

has been used for the two types of charge carriers. Moreover, since λ_s describes the reorganization of the surrounding medium induced by local charge hopping processes, it should also be correlated to the energetic disorder, i.e., to the changes in the polarization energies P^\pm along the PDI columns.

5.3. Comparison to Experiments. The charge carrier mobilities in these systems have been measured by Chen et al. in the crystal phase using the pulse-radiolysis time-resolved microwave conductivity (PR-TRMC) technique.³³ PR-TRMC measurements yield the sum of the positive and negative charge carrier mobilities, $\mu_{\text{TRMC}} = \mu_{\text{h+}} + \mu_{\text{e-}}$. The PR-TRMC method provides trap-free mobility values associated with well-organized domains within the material.^{56,57} Such mobilities can thus be regarded as an upper limit to the bulk values. In comparison, the measurement of TOF 1D-mobilities π -conjugated columnar stacks demands an extremely high degree of self-organization, with organization of the columns perfectly orthogonal to the electrode surface. Very good agreement between mobility values determined by PR-TRMC and TOF measurements has been found for the liquid crystalline phases of the mesomorphic discotic hexa(hexylthio)triphenylene molecule, which forms well-organized, interelectrode layers.⁵⁸

The reported PR-TRMC charge mobilities for the crystal phase of the PDI-based systems investigated here range between 0.14 and 0.42 $\text{cm}^2 \text{V}^{-1} \text{s}^{-1}$. In our simulations, the lower and higher limits for charge carriers mobilities are provided by the static (μ_{stat}) and dynamic (μ_{dyn}) limits, respectively. By taking the sum of the mobilities calculated for electrons and holes using the more realistic INDO transfer integrals, good agreement with the experimental values is only obtained in the static case and using rather large λ_s values (on the order of 0.2 eV). Mobility values that are typically 1 order of magnitude larger than PR-TRMC results are computed from INDO calculations in the dynamic limit (while in this limit the VB/HF results provide a more satisfactory agreement owing to the underestimated transfer integrals). Although the uncertainties on the model and on the parameters (in particular the reorganization energy) do not allow pulling out quantitative numbers, it is clear from our calculations that the charge carrier mobilities in the PDI stacks investigated here suffer from structural defects with lifetimes exceeding the residence times of the charge carriers (hence the

overall better agreement between the measured mobility values and those calculated in the static approach). This assertion is supported by analysis of the autocorrelation functions of the main geometrical parameters governing the magnitude of the transfer integrals, namely the twist angle θ , and the Δx and Δy shifts (see the Supporting Information). Exponential fits of the early time decay of these functions indeed yield (intermolecular) characteristic time scales on the order of 10^{-10} s, i.e., three orders of magnitude longer than the average residence time of the charge carriers on the PDI units (8×10^{-14} s and 6×10^{-13} s for holes and electrons, respectively).

6. CONCLUSIONS

Atomistic simulations based on the combination of classical force field and quantum-chemical calculations have been performed to assess the charge transport properties in a PDI derivative. The MD simulations show that the molecules self-organize in helicoidal columns that assemble in an hexagonal phase. The cell parameters and relative orientation of the molecules inside the columns are found to be in good agreement with X-ray diffraction data.

Based on these structural data, the energetic disorder has been evaluated as the change in electronic polarization energy of the charge as it moves along the stacks. We have shown that this energy is significantly impacted by the structural distortions of the environment, which is also the case for the transfer integrals mediating the charge hopping events. Hence, such fluctuations feed both diagonal and off-diagonal disorder. Calculations on model physical dimers have allowed identifying the structural parameters (namely, essentially a combination of lateral displacements and rotations) that contribute the most to the site energy and coupling distributions at room temperature.

Using such an energy landscape and the fluctuating transfer integrals, we have then assessed the charge carrier mobilities via time-of-flight numerical simulations. These calculations were based on a kinetic Monte Carlo scheme using Marcus-Jortner rates. Charge carrier mobility values spanning several orders of magnitude are predicted depending on the assumptions considered in the treatment of charge transport and molecular motion. As expected, much larger values of μ are obtained when considering a fast rearrangement in space and time of the PDI units, as compared to the static case. The experimental values seem to be in better agreement with the rigid structure simulations, but no decisive conclusions can be drawn at this stage owing to the uncertainty in the external reorganization energy and the simplicity of the hopping model used. Work along these lines is now in progress.

■ ASSOCIATED CONTENT

S Supporting Information. Complementary discussions, figures, and animations. This material is available free of charge via the Internet at <http://pubs.acs.org>.

■ ACKNOWLEDGMENT

The authors acknowledge the European projects MINOTOR (FP7-NMP-228424) and ONE-P (NMP3-LA-2008-212311) for financial support. The work in Mons is partly supported by the Interuniversity Attraction Pole IAP 6/27 of the Belgian Federal Government, and the Belgian National Fund for Scientific Research (FNRS/FRFC). N.M. acknowledges a grant from

"Fonds pour la Formation à la Recherche dans l'Industrie et dans l'Agriculture (FRIA)". J.C., Y.O., and D.B. are Research Fellows of FNRS. J.I. is grateful to the "Advanced Material in Aquitaine" program (www.ama-materials.com) for his Ph.D. grant. Calculations were carried out on mainframe computers of the "Mésocentre de Calcul Intensif Aquitain" (MCIA) of the University Bordeaux I financed by Conseil Régional d'Aquitaine and the French Ministry of Research and Technology, as well as on the Interuniversity Scientific Calculation Facility (ISCF) installed at Facultés Universitaires Notre-Dame de la Paix (Namur, Belgium), for which the authors gratefully acknowledge the financial support of FNRS-FRFC.

■ REFERENCES

- (1) Grozema, F.; Andrienko, D.; Kremer, K.; Müllen, K. *Nat. Mater.* **2009**, *8*, 421.
- (2) Kraft, A.; Grimsdale, A. C.; Holmes, A. B. *Angew. Chem., Int. Ed.* **1998**, *37*, 402.
- (3) Pan, J.; Zhu, W.; Li, S.; Zeng, W.; Cao, Y.; Tian, H. *Polymer* **2005**, *46*, 7658.
- (4) Breeze, A. J.; Salomon, A.; Ginley, D. S.; Gregg, B. A.; Tillmann, H.; Hörrhold, H.-H. *Appl. Phys. Lett.* **2002**, *81*, 3085.
- (5) Gregg, B. A.; et al. *Chem. Phys. Lett.* **1996**, *258*, 376.
- (6) Günster, S.; Siebentritt, S.; Meissner, D. *Mol. Cryst. Liquid Cryst.* **1993**, *229*, 111.
- (7) Panayotatos, P.; Bird, G.; Sauers, R.; Piechowski, A.; Husain, S. *Solar Cells* **1987**, *21*, 301.
- (8) Schmidt-Mende, L.; Fechtenkötter, A.; Müllen, K.; Moons, E.; Friend, R. H.; MacKenzie, J. D. *Science* **2001**, *293*, 1119.
- (9) Tang, C. W. *Appl. Phys. Lett.* **1986**, *48*, 183.
- (10) Tsuzuki, T.; Hirota, N.; Noma, N.; Shiota, Y. *Thin Solid Films* **1996**, *273*, 177.
- (11) Wöhrle, D.; Kreienhoop, L.; Schnurpfeil, G.; Elbe, J.; Tennigkeit, B.; Hiller, S.; Schlettwein, D. *J. Mater. Chem.* **1995**, *5*, 1819.
- (12) Bunk, O.; Nielsen, M. M.; Solling, T. I.; van de Craats, A. M.; Stutzmann, N. *J. Am. Chem. Soc.* **2003**, *125*, 2252.
- (13) Dimitrakopoulos, C. D.; Malenfant, P. R. L. *Adv. Mater.* **2002**, *14*, 99.
- (14) Jones, B. A.; Ahrens, M. J.; Yoon, M.-H.; Facchetti, A.; Marks, T. J.; Wasielewski, M. R. *Angew. Chem., Int. Ed.* **2004**, *116*, 6363.
- (15) Jones, B. A.; Facchetti, A.; Wasielewski, M. R.; Marks, T. J. *J. Am. Chem. Soc.* **2007**, *129*, 15259.
- (16) Malenfant, P. R. L.; Dimitrakopoulos, C. D.; Gelorme, J. D.; Kosar, L. L.; Graham, T. O. *Appl. Phys. Lett.* **2002**, 2517.
- (17) Würthner, F.; Schmidt, R. *ChemPhysChem* **2006**, *7*, 793.
- (18) Bayer, A.; Hübner, J.; Kopitzke, J.; Oestreich, M.; Rühe, W.; Wendorff, J. H. *J. Phys. Chem. A* **2001**, *105*, 4596.
- (19) Warman, J. M.; Van De Craats, A. M. *Mol. Cryst. Liq. Cryst.* **2003**, *396*, 41.
- (20) Craats, A. M. v. d.; Warman, J. M.; Fechtenkötter, A.; Brand, J. D.; Harbison, M. A.; Müllen, K. *Adv. Mater.* **1999**, *11*, 1469.
- (21) Craats, A. M. v. d.; Warman, J. M. *Adv. Mater.* **2001**, *13*, 130.
- (22) Chesterfield, R. J.; McKeen, J. C.; Newman, C. R.; Ewbank, P. C.; da Silva, D. A.; Bredas, J. L.; Miller, L. L.; Mann, K. R.; Frisbie, C. D. *J. Phys. Chem. B* **2004**, *108*, 19281–19292.
- (23) Pisula, W.; Feng, X.; Müllen, K. *Adv. Mater.* **2010**, *22*, 3634.
- (24) Ruiz Delgado, M. C.; Kim, E.-G.; da Silva Filho, D. A.; Brédas, J.-L. *J. Am. Chem. Soc.* **2010**, *132*, 3375.
- (25) Simpson, C. D.; Wu, J.; Watson, M. D.; Millen, K. *J. Mater. Chem.* **2004**, *14*, 494.
- (26) Tschierske, C. *J. Mater. Chem.* **1998**, *8*, 1485.
- (27) Würthner, F. *Chem. Commun.* **2004**, 1564.
- (28) Cornil, J.; Lemaury, V.; Calbert, J. P.; Brédas, J. L. *Adv. Mater.* **2002**, *14*, 726.
- (29) Crispin, X.; Cornil, J.; Friedlein, R.; Kamiya Okudaira, K.; Lemaury, V.; Crispin, A.; Kestemont, G.; Lehmann, M.; Fahlman, M.; Lazzaroni, R.; Geerts, Y.; Wendin, G.; Ueno, N.; Brédas, J. L.; Salaneck, W. R. *J. Am. Chem. Soc.* **2004**, *126* (38), 11889.
- (30) Lemaury, V.; Filho, D. A. d. S.; Coropceanu, V.; Lehmann, M.; Geerts, Y.; Piris, J.; Debije, M. G.; Craats, A. M. v. d.; Senthilkumar, K.; Siebbeles, L. D. A.; Warman, J. M.; Brédas, J.-L.; Cornil, J. *J. Am. Chem. Soc.* **2004**, *126*, 3271.
- (31) Palenberg, M. A.; Silbey, R. J.; Malagoli, M.; Brédas, J. L. *J. Chem. Phys.* **2000**, *112*, 1541.
- (32) Senthilkumar, K.; Grozema, F. C.; Bickelhaup, F. M.; Siebbeles, L. D. A. *J. Chem. Phys.* **2003**, *119*, 9809–9817.
- (33) Chen, Z.; Stepanenko, V.; Dehm, V.; Prins, P.; Siebbeles, L. D. A.; Seibt, J.; Marquetand, P.; Engel, V.; Würthner, F. *Chem.—Eur. J.* **2007**, *13*, 436.
- (34) Nelson, J.; Kwiatkowski, J. J.; Kirkpatrick, J.; Frost, J. M. *Acc. Chem. Res.* **2009**, *42*, 1768.
- (35) Olivier, Y.; Muccioli, L.; Lemaury, V.; Geerts, Y. H.; Zannoni, C.; Cornil, J. *J. Phys. Chem. B* **2009**, *113*, 14102.
- (36) Tinker 5.1, <http://dasher.wustl.edu/tinker/>.
- (37) Allinger, N. L. *J. Am. Chem. Soc.* **1977**, *99*, 8127.
- (38) Jortner, J. *J. Chem. Phys.* **1976**, *64*, 4860.
- (39) Marcus, R. A. *Rev. Mod. Phys.* **1993**, *65*, 599.
- (40) Coropceanu, V.; Malagoli, M.; da Silva Filho, D. A.; Gruhn, N. E.; Bill, T. G.; Brédas, J. L. *Phys. Rev. Lett.* **2002**, *89*, 275503.
- (41) McMahon, D. P.; Troisi, A. *J. Phys. Chem. Lett.* **2010**, *1*, 941.
- (42) Martinelli, N. G.; Idé, J.; Sánchez-Carrera, R. S.; Coropceanu, V.; Brédas, J. L.; Ducasse, L.; Castet, F.; Cornil, J.; Beljonne, D. *J. Phys. Chem. C* DOI: 10.1021/jp105843t.
- (43) Castet, F.; Aurel, P.; Fritsch, A.; Ducasse, L.; Liotard, D.; Linares, M.; Cornil, J.; Beljonne, D. *Phys. Rev. B* **2008**, *77*, 115210.
- (44) Brédas, J. L.; Beljonne, D.; Coropceanu, V.; Cornil, J. *Chem. Rev.* **2004**, *104*, 4971.
- (45) Olivier, Y.; Lemaury, V.; Brédas, J. L.; Cornil, J. *J. Phys. Chem. A* **2006**, *110* (19), 6356.
- (46) Voter, A. F. Introduction to the Kinetic Monte Carlo Method in Radiation Effects in Solids. In *NATO Science Series II: Mathematics, Physics and Chemistry*; Sickafus, K. E., Kotomin, E. A., Uberuaga, B. P., Eds.; NATO: 2007; Vol. 235.
- (47) Adam, D.; Closs, F.; Frey, T.; Funhoff, D.; Haarer, D.; Schuhmacher, P.; Siemensmeyer, K. *Phys. Rev. Lett.* **1993**, *70*, 457.
- (48) Kirkpatrick, J.; Marcon, V.; Nelson, J.; Kremer, K.; Andrienko, D. *Phys. Rev. Lett.* **2007**, *98*, 227402.
- (49) Berendsen, H. J. C.; Postma, J. P. M.; van Gunsteren, W. F.; DiNola, A.; Haak, J. R. *J. Chem. Phys.* **1984**, *81*, 3684.
- (50) Percec, V.; Ahn, C.-H.; Bera, T. K.; Unger, G.; Yeardley, D. J. P. *Chem.—Eur. J.* **1999**, *5*, 1070.
- (51) Ghosh, S.; Li, X.-Q.; Stepanenko, V.; Würthner, F. *Chem.—Eur. J.* **2008**, *14*, 11343–11357.
- (52) Vura-Weis, J.; Ratner, M. A.; Wasielewski, M. R. *J. Am. Chem. Soc.* **2010**, *132*, 1738.
- (53) Castet, F.; Ducasse, L.; Fritsch, A. *Chem. Phys.* **1998**, *232*, 37.
- (54) Brunaud, G.; Castet, F.; Fritsch, A.; Kreissler, M.; Ducasse, L. *J. Phys. Chem. B* **2001**, *105*, 12665.
- (55) Coropceanu, V.; Cornil, J.; da Silva Filho, D. A.; Olivier, Y.; Silbey, R.; Brédas, J. L. *Chem. Rev.* **2007**, *107*, 926.
- (56) Horowitz, G.; Kouki, F.; Spearman, P.; Fichou, D.; Nogues, C.; Pan, X.; Garnier, F. *Adv. Mater.* **1996**, *8*, 242–245.
- (57) Meyer, J.-P.; Schlettwein, D.; Wöhrle, D.; Jaeger, N. I. *Thin Solid Films* **1995**, *258*, 317.
- (58) Craats, A. M. v. d.; Warman, J. M.; de Haas, M. P.; Adam, D.; Simmerer, J.; Haarer, D.; Schuhmacher, P. I. *Adv. Mater.* **1996**, *8*, 823–826.